Journal of Zhejiang University-SCIENCE A (Applied Physics & Engineering)
ISSN 1673-565X (Print); ISSN 1862-1775 (Online)
www.jzus.zju.edu.cn; www.springerlink.com
E-mail: jzus@zju.edu.cn

Numerical investigation of flow characteristics around two side-by-side cylinders by immersed boundary-lattice Boltzmann flux solver

Xiao-di WU†, Hua-ping LIU, Fu CHEN

Department of Energy Science and Engineering, Harbin Institute of Technology, Harbin 150001, China

†E-mail: wuxiaodi528@163.com

Received Mar. 5, 2017; Revision accepted July 3, 2017; Crosschecked Apr. 13, 2018

Abstract: In this paper, to study the characteristics of the flow in a laminar regime, an immersed boundary-lattice Boltzmann flux solver (IB-LBFS) is applied to numerically simulate the unsteady viscous flows around two fixed and rotating circular cylinders in side-by-side arrangement. This method applies finite volume discretization to solve the macroscopic governing equations with the flow variables defined at cell centers. At the cell interface, numerical fluxes are physically evaluated by a local lattice Boltzmann solution. In addition, the no-slip boundary condition is accurately imposed by using the implicit boundary condition-enforced immersed boundary method. Due to the simplicity and high efficiency of IB-LBFS on non-uniform grids, it is suitable for simulating fluid flows with complex geometries and moving boundaries. Firstly, numerical simulations of laminar flow past two side-by-side cylinder are performed with different gap spacings at Reynolds numbers of 100 and 200. The simulation results show that a small gap spacing induces a biased flow and forms an irregular big wake behind two cylinders at a low Reynolds number. As the gap spacing increases, an in-phase or anti-phase flow is observed. Then, the effects of the main important parameters on flow characteristics are analyzed for flow past two side-by-side rotating cylinders, including the rotational speed, Reynolds number, and gap spacing. As the rotational speed is increased, the numerical results illustrate that unsteady wakes are suppressed and the flow becomes steady. As the gap spacing is increased, two separate vortex streets behind each cylinder are formed with a definite phase relationship and single shedding frequency.

Key words: Immersed boundary method (IBM); Lattice Boltzmann flux solver (LBFS); Moving boundary; Side-by-side cylinders
https://doi.org/10.1631/jzus.A1700112 **CLC number:** O35

1 Introduction

Flow around multiple bluff bodies in different arrangements plays an important role in various engineering applications, such as offshore platforms, transmission cables, external ballistics, and ship stabilization (Supradeepan and Roy, 2015). The complex configuration and moving boundary behavior of fluid flow in such situations pose several challenges from experimental, theoretical, and computational aspects (Kumar et al., 2011). The flow around two circular cylinders in a side-by-side arrangement, as a canonical problem, is applicable for understanding the characteristics of flow around multiple bluff bodies. With different spacing ratios and Reynolds numbers, the phenomenon of vortex shedding from cylinders becomes more complex. To achieve a rational structure design, it is necessary to understand the flow characteristics of interactions of multiple bluff bodies, and be able to predict the force and response of the cylinder-like structures (Ding et al., 2007). Therefore, it is critical to control the wake behind cylinders appropriately in practical engineering environments, especially for the purpose of suppressing vortex shedding.

ORCID: Xiao-di WU, https://orcid.org/0000-0001-5631-7216

Many experiments have been carried out to observe the wake characteristics of the flow past side-by-side circular cylinders by laser-illuminated flow-visualization, particle image velocimetry (PIV), and hot-wire measurements. For two stationary cylinders of equal diameters, there are mainly three wake regimes, including single street (L/D<1.2), asymmetrical flow (1.2<L/D<2.0), and two-coupled street (L/D>2.0), where L is the cylinder center-to-center distance and D is the cylinder diameter (Wang and Zhou, 2005). For two stationary cylinders of unequal diameters, the wake structure was studied by Gao et al. (2010) and Song et al. (2015). For flow past two rotating cylinders with the same rotation rates, the effects of different Reynolds numbers and non-dimensional rotation speeds on wake structure were analyzed (Kumar et al., 2011). The experimental investigation has been performed for a single spacing ratio of L/D=2.5 during the occurrence of a self-excited acoustic resonance condition in the duct (Mohany et al., 2014).

Alongside the experiments, the main research approach is a numerical simulation method to solve the macroscopic Navier-Stokes (N-S) equations. There have been many attempts using different numerical approaches to analyze the flow characteristics of two side-by-side circular cylinders. Ding et al. (2007) simulated the flows by mesh-free least square-based finite difference methods. Vakil and Green (2011) used a direct numerical simulation method. Hesam et al. (2011) adopted a Cartesian grid finite volume method. Moreover, the no-slip condition on the curved boundaries of cylinders was applied by using the ghost-cell method (Behzad and Hamed, 2009). Supradeepan and Roy (2014) used a finite volume consistent flux reconstruction scheme for an unstructured grid. In conclusion, numerical simulations mainly focus on the effects of the main important parameters, including Reynolds number and gap spacing, on the flow characteristics.

Recently, the lattice Boltzmann equation (LBE), as a mesoscopic approach, has attracted more attention as an available alternative for solving flow problems. It has the following advantages: the macroscopic variables can be easily solved by distribution functions; the linear streaming and collision processes can effectively simulate the nonlinear convection and diffusion effects in the macroscopic state. However, the standard LBE is limited to a simple geometric configuration and uniform Cartesian mesh due to the lattice uniformity for incompressible flow and it can simulate the viscous flow. Based on the above analysis, Shu et al. (2015) developed a lattice Boltzmann flux solver (LBFS) for simulating incompressible flows in order to combine the merits of N-S solvers and LBE solvers. For flow past bluff bodies, the boundary condition plays an essential role. Usually, a body-fitted mesh is employed, which involves coordinate transformation and new mesh generation at every time step. The immersed boundary method (IBM) is an effective technique for solving the problems with non-body conforming Cartesian grid. For the boundary treatment of the IBM, the key point is to calculate the forcing density on Lagrangian points which must ensure boundary conditions. Usually, the penalty force method and direct forcing method (Feng and Michaelides, 2004, 2005) are applied to evaluate the force. However, these methods can not satisfy the no-slip boundary condition. Therefore, the boundary condition-enforced IBM, which was proposed by Wu and Shu (2009, 2010), is adopted due to its accuracy in satisfying the no-slip boundary condition and avoiding streamlines penetrating of the solid body. Wang et al. (2015a, 2016, 2017) developed a new numerical method called immersed boundary-lattice Boltzmann flux solver (IB-LBFS), which combined LBFS and boundary condition-enforced IBM, to simulate incompressible flow.

In this paper, we attempt to adopt IB-LBFS to study the flow characteristics of flows past two side-by-side circular cylinders. The IB-LBFS has been proven to be an efficient solver for simulating incompressible flows on non-uniform grids, with a flexible way of treating the no-slip boundary condition by immersed boundary technology. This method provides an effective, flexible, and simple pathway to deal with complex structure and moving boundary problems.

2 Numerical methods

2.1 Immersed boundary-lattice Boltzmann flux solver

The IB-LBFS (Wang et al., 2015a, 2016, 2017) is suitable for simulating flows with complex

geometries and moving boundary problems. By applying the fractional step method, the IB-LBFS decouples the solution of government equations into two steps: the predictor step and the corrector step. LBFS is implemented in the predictor step and the boundary condition-enforced IBM is applied in the corrector step.

For incompressible viscous flows, the macroscopic N-S equations with IBM can be written as

$$\frac{\partial \rho}{\partial t}+\nabla\cdot\rho\boldsymbol{u}=0, \tag{1}$$

$$\frac{\partial \rho\boldsymbol{u}}{\partial t}+\nabla(\rho\boldsymbol{u}\boldsymbol{u})=-\nabla p+\nabla\left[\mu(\nabla\boldsymbol{u}+(\nabla\boldsymbol{u})^{\mathrm{T}})\right]+\boldsymbol{f}, \tag{2}$$

where ρ, $\boldsymbol{u}$, p, μ, and $\boldsymbol{f}$ represent the fluid density, fluid velocity, fluid pressure, dynamic viscosity coefficient, and a restoring force given by the IBM, respectively.

Based on the multi-scale Chapman-Enskog analysis, the fluxes in Eqs. (1) and (2) can be evaluated by LBFS with the following relationships (Shu et al., 2015; Wang et al., 2015b),

$$\rho\boldsymbol{u}=\sum_{\alpha}\boldsymbol{e}_{\alpha}f_{\alpha}^{\mathrm{eq}}, \tag{3}$$

$$\begin{aligned}&\rho\boldsymbol{u}\boldsymbol{u}+p-\mu\left[\nabla\boldsymbol{u}+(\nabla\boldsymbol{u})^{\mathrm{T}}\right]\\&\quad=\sum_{\alpha}(\boldsymbol{e}_{\alpha})_{\beta}(\boldsymbol{e}_{\alpha})_{\gamma}\left[f_{\alpha}^{\mathrm{eq}}+\left(1-\frac{1}{2\tau}\right)f_{\alpha}^{\mathrm{neq}}\right],\end{aligned} \tag{4}$$

$$f_{\alpha}^{\mathrm{neq}}=-\tau\delta_{\mathrm{t}}\left(\frac{\partial}{\partial t}+\boldsymbol{e}_{\alpha}\cdot\nabla\right)f_{\alpha}^{\mathrm{eq}}, \tag{5}$$

where α is the direction of lattice velocity; $\boldsymbol{e}_{\alpha}$ is the particle velocity in the α direction; β and γ are the coordinate directions; f_{α}^{eq} and $f_{\alpha}^{\mathrm{neq}}$ are the equilibrium density distribution function and the non-equilibrium term, respectively; τ is the single relaxation parameter which can be expressed as $\tau=\mu/(\rho c_{\mathrm{s}}^{2}\delta_{\mathrm{t}})+0.5$. c_{s} is the sound speed of model and $c_{\mathrm{s}}=c/\sqrt{3}$, where $c=\delta_x/\delta_{\mathrm{t}}$, δ_x and δ_{t} are the lattice intervals in space and time steps.

For the 2D case, the most popular lattice velocity model is the D2Q9 model (Qian *et al*., 1992) which is shown in Fig. 1 and the velocity is given by

$$\boldsymbol{e}_{\alpha}=\begin{cases}0, & \alpha=0,\\ (\cos[(\alpha-1)\pi/2],\\ \quad\sin[(\alpha-1)\pi/2])c, & \alpha=1,2,3,4,\\ \sqrt{2}(\cos[(\alpha-5)\pi/2+\pi/4],\\ \quad\sin[(\alpha-5)\pi/2+\pi/4])c, & \alpha=5,6,7,8.\end{cases} \tag{6}$$

The corresponding equilibrium density distribution function, the LBGK (lattice Bhatnagar-Gross-Krook) model, is

$$f_{\alpha}^{\mathrm{eq}}(\boldsymbol{r},t)=\rho w_{\alpha}\left[1+\frac{\boldsymbol{e}_{\alpha}\cdot\boldsymbol{u}}{c_{\mathrm{s}}^{2}}+\frac{(\boldsymbol{e}_{\alpha}\cdot\boldsymbol{u})^{2}-\left(c_{\mathrm{s}}|\boldsymbol{u}|\right)^{2}}{2c_{\mathrm{s}}^{4}}\right], \tag{7}$$

with the coefficients w_0=4/9; w_1=w_2=w_3=w_4=1/9; w_5=w_6=w_7=w_8=1/36. $\boldsymbol{r}$ represents the physical location and t is the time.

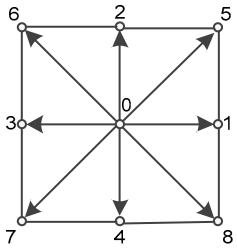

Fig. 1 Discrete velocities of the D2Q9 model on a 2D square lattice

After including a forcing density term generated by the boundary effect, the overall governing equations of the IB-LBFS can be written as

$$\frac{\partial \rho}{\partial t}+\nabla\cdot\left(\sum_{\alpha}\boldsymbol{e}_{\alpha}f_{\alpha}^{\mathrm{eq}}\right)=0, \tag{8}$$

$$\frac{\partial \rho\boldsymbol{u}}{\partial t}+\nabla\cdot\boldsymbol{\Pi}=\boldsymbol{f}, \tag{9}$$

where

$$\boldsymbol{\Pi}=\sum_{\alpha}(\boldsymbol{e}_{\alpha})_{\beta}(\boldsymbol{e}_{\alpha})_{\gamma}\left[f_{\alpha}^{\mathrm{eq}}+\left(1-\frac{1}{2\tau}\right)f_{\alpha}^{\mathrm{neq}}\right], \tag{10}$$

$$f_{\alpha}^{\mathrm{neq}}=-\tau\delta_{\mathrm{t}}\left(\frac{\partial}{\partial t}+\boldsymbol{e}_{\alpha}\cdot\nabla\right)f_{\alpha}^{\mathrm{eq}}. \tag{11}$$

The solution process of Eqs. (8) and (9) can be split into two steps:

1. Predictor step

$$\frac{\rho^{n+1}-\rho^{n}}{\Delta t}+\nabla\cdot\left(\sum_{\alpha}\boldsymbol{e}_{\alpha}f_{\alpha}^{\mathrm{eq}}\right)=0, \tag{12}$$

$$\frac{\rho^{n+1}\boldsymbol{u}^{*}-\rho^{n}\boldsymbol{u}^{n}}{\Delta t}+\nabla\cdot\boldsymbol{\Pi}=0; \tag{13}$$

2. Corrector step

$$\frac{\rho^{n+1}(\boldsymbol{u}^{n+1}-\boldsymbol{u}^{*})}{\Delta t}=\boldsymbol{f}, \tag{14}$$

where $\boldsymbol{u}^{*}$ is an intermediate velocity; n represents the nth step. The details of two steps are presented below.

2.2 Lattice Boltzmann flux solver

Using the finite volume method, Eqs. (12) and (13) can be discretized as follows:

$$\frac{\mathrm{d}\boldsymbol{W}_{i}}{\mathrm{d}t}+\frac{1}{\mathrm{d}V_{i}}\sum_{k}\boldsymbol{R}_{k}\mathrm{d}S_{k}=0, \tag{15}$$

where $\boldsymbol{W}=[\rho,\rho\boldsymbol{u}]^{\mathrm{T}}$, $\mathrm{d}V_{i}$ is the volume of the ith control, and $\mathrm{d}S_{k}$ is the area of the kth interface. For the D2Q9 lattice velocity model, the fluxes can be written as

$$\boldsymbol{R}_{k}=\begin{pmatrix} n_{x}\left(f_{1}^{\mathrm{eq}}-f_{3}^{\mathrm{eq}}+f_{5}^{\mathrm{eq}}-f_{6}^{\mathrm{eq}}-f_{7}^{\mathrm{eq}}+f_{8}^{\mathrm{eq}}\right)\\ \quad+n_{y}\left(f_{2}^{\mathrm{eq}}-f_{4}^{\mathrm{eq}}+f_{5}^{\mathrm{eq}}+f_{6}^{\mathrm{eq}}-f_{7}^{\mathrm{eq}}-f_{8}^{\mathrm{eq}}\right)\\ n_{x}\left(f_{1}^{\wedge}+f_{3}^{\wedge}+f_{5}^{\wedge}+f_{6}^{\wedge}+f_{7}^{\wedge}+f_{8}^{\wedge}\right)\\ \quad+n_{y}\left(f_{5}^{\wedge}-f_{6}^{\wedge}+f_{7}^{\wedge}-f_{8}^{\wedge}\right)\\ n_{x}\left(f_{5}^{\wedge}-f_{6}^{\wedge}+f_{7}^{\wedge}-f_{8}^{\wedge}\right)\\ \quad+n_{y}\left(f_{2}^{\wedge}+f_{4}^{\wedge}+f_{5}^{\wedge}+f_{6}^{\wedge}+f_{7}^{\wedge}+f_{8}^{\wedge}\right) \end{pmatrix}, \tag{16}$$

where

$$f_{\alpha}^{\wedge}=f_{\alpha}^{\mathrm{eq}}+\left(1-\frac{1}{2\tau}\right)f_{\alpha}^{\mathrm{neq}}, \tag{17}$$

where $\boldsymbol{n}=(n_x, n_y)$ is the unit normal vector on the control surface. Using the Taylor series expansion, the non-equilibrium density distribution function can be derived:

$$f_{\alpha}^{\mathrm{neq}}(\boldsymbol{r},t)=-\tau\left[f_{\alpha}^{\mathrm{eq}}(\boldsymbol{r},t)-f_{\alpha}^{\mathrm{eq}}(\boldsymbol{r}-\boldsymbol{e}_{\alpha}\delta_{\mathrm{t}},t-\delta_{\mathrm{t}})\right]. \tag{18}$$

Thus, the fluxes can be calculated by solving the equilibrium distribution function $f_{\alpha}^{\mathrm{eq}}(\boldsymbol{r}-\boldsymbol{e}_{\alpha}\delta_{\mathrm{t}},t-\delta_{\mathrm{t}})$ and $f_{\alpha}^{\mathrm{eq}}(\boldsymbol{r},t)$.

From Fig. 2, the flow properties of eight vertices of the D2Q9 model can be evaluated by interpolation with the given flow properties at the cell centers of two adjacent control volumes (V_i and V_{i+1}). The interpolation formulation can be given as

$$\psi(\boldsymbol{r}-\boldsymbol{e}_{\alpha}\delta_{\mathrm{t}},t-\delta_{\mathrm{t}})=\begin{cases}\psi(\boldsymbol{r}_{i})+(\boldsymbol{r}-\boldsymbol{e}_{\alpha}\delta_{\mathrm{t}}-\boldsymbol{r}_{i})\cdot\nabla\psi(\boldsymbol{r}_{i}), & \boldsymbol{r}-\boldsymbol{e}_{\alpha}\delta_{\mathrm{t}}\ \text{in}\ V_{i},\\ \psi(\boldsymbol{r}_{i+1})+(\boldsymbol{r}-\boldsymbol{e}_{\alpha}\delta_{\mathrm{t}}-\boldsymbol{r}_{i+1})\cdot\nabla\psi(\boldsymbol{r}_{i+1}), & \boldsymbol{r}-\boldsymbol{e}_{\alpha}\delta_{\mathrm{t}}\ \text{in}\ V_{i+1},\end{cases} \tag{19}$$

where $\boldsymbol{r}_i$, $\boldsymbol{r}_{i+1}$, and $\boldsymbol{r}$ are the physical locations for the two cell centers and their interface, respectively. After that, $f_{\alpha}^{\mathrm{eq}}(\boldsymbol{r}-\boldsymbol{e}_{\alpha}\delta_{\mathrm{t}},t-\delta_{\mathrm{t}})$ can be obtained according to Eq. (7).

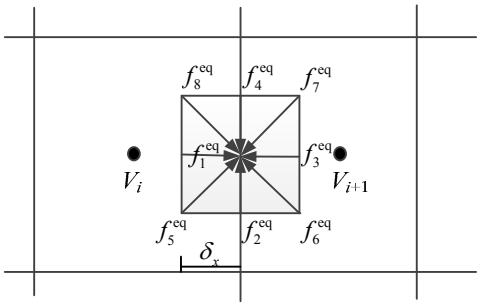

Fig. 2 Local flux reconstruction at cell interface

The reconstructed flow variables at the interface by the LBE solutions are as follows:

$$\rho(\boldsymbol{r},t)=\sum_{\alpha=0}^{8}f_{\alpha}^{\mathrm{eq}}(\boldsymbol{r}-\boldsymbol{e}_{\alpha}\delta_{\mathrm{t}},t-\delta_{\mathrm{t}}), \tag{20}$$

$$\rho(\boldsymbol{r},t)u(\boldsymbol{r},t)=\sum_{\alpha=0}^{8}\boldsymbol{e}_{\alpha}f_{\alpha}^{\mathrm{eq}}(\boldsymbol{r}-\boldsymbol{e}_{\alpha}\delta_{\mathrm{t}},t-\delta_{\mathrm{t}}). \tag{21}$$

Then, $f_{\alpha}^{\mathrm{eq}}(\boldsymbol{r},t)$ can be easily solved by Eq. (7). After obtaining $f_{\alpha}^{\mathrm{eq}}(\boldsymbol{r}-\boldsymbol{e}_{\alpha}\delta_{\mathrm{t}},t-\delta_{\mathrm{t}})$ and $f_{\alpha}^{\mathrm{eq}}(\boldsymbol{r},t)$, $f_{\alpha}^{\wedge}$ can be computed by Eq. (17) and the fluxes can be evaluated according to Eq. (16). Therefore, the flow field variables ρ^{n+1} and $\boldsymbol{u}^{*}$ can be solved in the predictor step.

2.3 Boundary condition-enforced IBM for velocity correction

For an intermediate velocity $\boldsymbol{u}^*$, a velocity correction is performed by applying boundary condition-enforced IBM (Wu and Shu, 2009). Compared with the explicit IBMs such as the penalty force and direct forcing methods which can only approximately satisfy the no-slip conditions, the boundary condition-enforced IBM can accurately satisfy the no-slip boundary condition. Based on the IBM, the computational domain is shown in Fig. 3, which includes Eulerian and Lagrangian points.

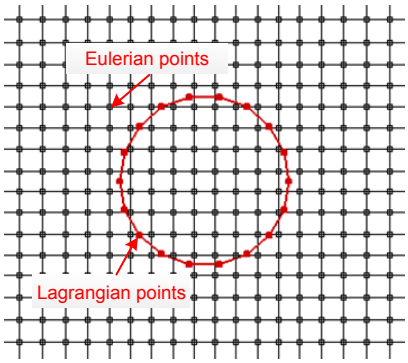

Fig. 3 A solid boundary immersed in a computational domain

If we define the velocity $\boldsymbol{u}^{n+1}$ as

$$\boldsymbol{u}^{n+1}=\boldsymbol{u}^*+\Delta\boldsymbol{u}, \tag{22}$$

then the velocity correction $\Delta\boldsymbol{u}$ at the Eulerian point can be obtained by the following Dirac delta function interpolation:

$$\Delta\boldsymbol{u}(r_j)=\sum_l \Delta\boldsymbol{u}_{\mathrm{B}}^l\Delta s^l\cdot D(\boldsymbol{r}_j-\boldsymbol{X}_{\mathrm{B}}^l),\quad l=1,2,\cdots,N, \tag{23}$$

where j is the jth Eulerian point; $\Delta\boldsymbol{u}_{\mathrm{B}}^l$ is the velocity correction of Lagrangian points and the subscript B stands for solid boundary; Δs^l is the unit length; $\boldsymbol{X}_{\mathrm{B}}^l$ and N are the position and number of Lagrangian points; $D(\ )$ is a continuous kernel function given by

$$D(\boldsymbol{r}_j-\boldsymbol{X}_{\mathrm{B}}^l)=\delta(r_j^x-x_{\mathrm{B}}^l)\cdot\delta(r_j^y-y_{\mathrm{B}}^l)/h^2, \tag{24}$$

$$\delta(r)=\begin{cases}(1+\cos(\pi|r|/2))/4, & |r|\le 2,\\ 0, & |r|>2,\end{cases} \tag{25}$$

where r_j^x and r_j^y are the positions of the jth Eulerian points in x and y coordinate directions, respectively; x_{B}^l and y_{B}^l are the position coordinates of Lagrangian points in x and y directions, respectively; h is the grid size of uniform mesh.

To guarantee the no-slip boundary conditions, the velocities of the Lagrangian points must be identical to those fluid velocities at the same positions. The velocity of the kth Lagrangian point can be obtained through interpolations of the corrected velocities of the Eulerian points:

$$\boldsymbol{U}^{n+1}(\boldsymbol{X}_{\mathrm{B}}^k)=\sum_j \boldsymbol{u}^{n+1}(\boldsymbol{r}_j)\cdot D(\boldsymbol{r}_j-\boldsymbol{X}_{\mathrm{B}}^k)h^2, \tag{26}$$

where $j=1,2,\cdots,M$, and M is the number of Eulerian points. Eqs. (22) and (23) are substituted into Eq. (26) to give

$$\begin{aligned}\boldsymbol{U}^{n+1}(\boldsymbol{X}_{\mathrm{B}}^k)=&\sum_j \boldsymbol{u}^*(\boldsymbol{r}_j)\cdot D(\boldsymbol{r}_j-\boldsymbol{X}_{\mathrm{B}}^k)h^2\\ &+\sum_j\left(\sum_l \Delta\boldsymbol{u}_{\mathrm{B}}^l\Delta s^l\cdot D(\boldsymbol{r}_j-\boldsymbol{X}_{\mathrm{B}}^l)\right)D(\boldsymbol{r}_j-\boldsymbol{X}_{\mathrm{B}}^k)h^2.\end{aligned} \tag{27}$$

If we take $\Delta\boldsymbol{u}_{\mathrm{B}}^l\Delta s^l$ as unknowns, the above equation system can be rewritten in a matrix form:

$$\boldsymbol{A}\boldsymbol{X}=\boldsymbol{B}, \tag{28}$$

where

$$\begin{aligned}&\boldsymbol{X}=\left[\Delta\boldsymbol{u}_{\mathrm{B}}^1\Delta s^1,\Delta\boldsymbol{u}_{\mathrm{B}}^2\Delta s^2,\cdots,\Delta\boldsymbol{u}_{\mathrm{B}}^N\Delta s^N\right]^{\mathrm{T}},\\ &\boldsymbol{A}=h^2\begin{bmatrix}D_{11}&D_{12}&\cdots&D_{1M}\\D_{21}&D_{22}&\cdots&D_{2M}\\\vdots&\vdots&\ddots&\vdots\\D_{N1}&D_{N2}&\cdots&D_{NM}\end{bmatrix}\begin{bmatrix}D_{11}&D_{12}&\cdots&D_{1N}\\D_{21}&D_{22}&\cdots&D_{2N}\\\vdots&\vdots&&\vdots\\D_{M1}&D_{M2}&\cdots&D_{MN}\end{bmatrix},\\ &\boldsymbol{B}=\begin{bmatrix}\boldsymbol{U}_{\mathrm{B}}^1\\\boldsymbol{U}_{\mathrm{B}}^2\\\vdots\\\boldsymbol{U}_{\mathrm{B}}^N\end{bmatrix}^{n+1}-\begin{bmatrix}D_{11}&D_{12}&\cdots&D_{1M}\\D_{21}&D_{22}&\cdots&D_{2M}\\\vdots&\vdots&&\vdots\\D_{N1}&D_{N2}&\cdots&D_{NM}\end{bmatrix}\begin{bmatrix}\boldsymbol{u}_1^*\\\boldsymbol{u}_2^*\\\vdots\\\boldsymbol{u}_M^*\end{bmatrix}.\end{aligned} \tag{29}$$

The linear system of Eq. (28) is solved by a direct method so that the unknowns $\Delta\boldsymbol{u}_{\mathrm{B}}^k\Delta s^k$ at all Lagrangian points can be obtained simultaneously.

As pointed out by Lai and Peskin (2000), the drag force arises from two sources: the shear stress and the pressure distribution along the body. In the present work, the force can be directly computed from the velocity correction. The drag and lift coefficients are defined as

$$C_{\mathrm{d}}=\frac{2F_{\mathrm{D}}}{\rho U_{\infty}^{2}D},\quad F_{\mathrm{D}}=-\int_{\Gamma}f_{x}\mathrm{d}x, \tag{30}$$

$$C_{\mathrm{l}}=\frac{2F_{\mathrm{L}}}{\rho U_{\infty}^{2}D},\quad F_{\mathrm{L}}=-\int_{\Gamma}f_{y}\mathrm{d}x, \tag{31}$$

where f_x is the x component of force density and f_y is the y component; F_{D} and F_{L} are the drag and lift forces, respectively; Γ stands for the solid boundary; U_{∞} is the free stream velocity; D is the cylinder diameter.

For the unsteady flow, the Strouhal number S_{t} is defined as the dimensionless frequency f with which the vortices are shed from the body.

$$S_{\mathrm{t}}=f\cdot D/U_{\infty}. \tag{32}$$

2.4 Computational sequence

The complete numerical procedures for each time step of the proposed IB-LBFS method are summarized as follows.

1. Identify a streaming time step at each interface and then the single relaxation parameter at each interface can be computed;

2. Apply the D2Q9 model to compute the equilibrium density distribution function $f_{\alpha}^{\mathrm{eq}}(\boldsymbol{r}-\boldsymbol{e}_{\alpha}\delta_{\mathrm{t}}, t-\delta_{\mathrm{t}})$ at the positions $(\boldsymbol{r}-\boldsymbol{e}_{\alpha}\delta_{\mathrm{t}},t-\delta_{\mathrm{t}})$ around the middle point $\boldsymbol{r}$ of each interface;

3. Compute the macroscopic flow properties ρ and u at the cell interface and then compute f_{α}^{eq} and $f_{\alpha}^{\mathrm{neq}}$;

4. Compute the fluxes at the cell interface and predict the intermediate velocity $\boldsymbol{u}^{*}$;

5. Perform a velocity correction to obtain $\boldsymbol{u}^{n+1}$ by applying boundary condition-enforced IBM.

3 Numerical validations

To validate the accuracy of the IB-LFBS, the flows past a single stationary (Ω=0) and rotating cylinder ($\Omega\neq$0) are simulated (Fig. 4), where Ω is the angular velocity of the cylinder. The problem has been studied extensively and there are many theoretical, experimental, and numerical results available in the literature.

Both flows past stationary and rotating cylinders are in the laminar regimes with a low Reynolds number which is defined as $Re=\rho U_{\infty}D/\mu$. The computational domain is $[-40D,60D]\times[-40D,40D]$, and the center of the cylinder is located at 40D from the inlet boundary, 60D from the outlet boundary, and 40D from both top and bottom boundaries.

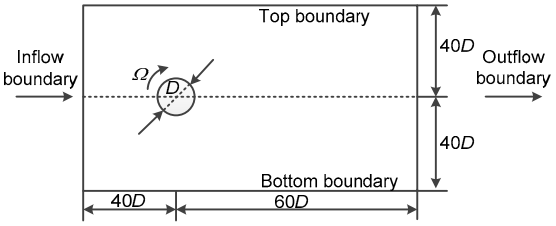

Fig. 4 Computational domain of 2D circular cylinder

3.1 Flow past a stationary cylinder

In the present simulation, unsteady (Re=100 and 200) flows past a stationery cylinder are studied. The flow and geometrical parameters are set as ρ=1.0, U_{∞}=0.1, and D=1.0. Free stream flow properties are applied at the inflow boundary and a natural boundary condition is used on top, bottom, and outflow boundaries. The no-slip boundary condition of the cylinder surface is imposed by the IBM. The solid boundary is represented by 150 Lagrangian points with a uniform distribution. A non-uniform mesh is used for the whole computational domain with a mesh size of 488×542. The cylinder is placed in a small square region with a uniform grid of 100×100. The force coefficients and the Strouhal number obtained by the present method are compared with previous results in Table 1. From the table, it can be seen that the present results agree well with those in the literature.

The number of Lagrangian points was decided based on a grid independence study carried out on the flows at Re=100 with six different numbers of Lagrangian points (80, 100, 120, 150, 180, and 200). The mean drag coefficient, the maximum drag coefficient, and Strouhal number are shown in Table 2.

From that table, it can be seen that the variation gradually become steady when the number of Lagrangian points is equal to or more than 120. Therefore, the number of 150 Lagrangian points is chosen to balance the computational accuracy and efficiency for all the simulations in this study.

3.2 Flow past a rotating cylinder

Flows past a rotating cylinder (Re=100) with different angular velocities are studied here. The flow and geometrical parameters are set as ρ=1.0, U_∞=0.1, and D=1.0. As moving boundary problem, η is an important parameter, which is the rotational speed at the cylinder surface normalized by the free-stream velocity. η is defined as $\eta=\Omega D/(2U_\infty)$. The solid boundary of this cylinder is also realized with 150 Lagrangian points with uniform distribution. Three different rotational speeds (0.5, 1.5, and 2.5) are applied to examine its effects on the flow pattern. A grid size of 470×460 with non-uniform distribution is used, and the cylinder is placed in a small square region with a uniform grid of 200×200.

The time-averaged drag and lift coefficients and the Strouhal number obtained by the present method are compared with the previous results in Table 3. From the table, it is seen that the present results agree well with those in the literature. Fig. 5 shows the vorticity (ω) contours for flow past a rotating cylinder with different rotational speeds. When the rotational speed η is small, the Karman vortex street is distinctly observed behind the cylinder. As η increases to 2.5, the Karman vortex street gradually disappears. From Table 3, it can be seen that drag coefficient on the cylinder reduces and simultaneously the lift coefficient is raised as η increases. This physical phenomenon is consistent with the previous findings.

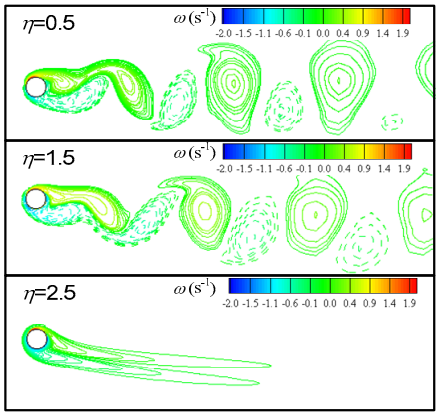

Fig. 5 Vorticity contours for flow past a rotating cylinder

Table 1 Drag and lift coefficients, and Strouhal number for flow over a stationary cylinder

Study	Re=100			Re=200		
	C_d	C_l	S_t	C_d	C_l	S_t
Liu et al. (1998)	1.35±0.012	±0.339	0.165	1.31±0.049	±0.690	0.192
Choi et al. (2007)	1.34±0.011	±0.315	0.164	1.36±0.048	±0.640	0.191
Harichandan and Roy (2010)	1.35±0.010	±0.278	0.161	1.32±0.050	±0.602	0.192
Supradeepan and Roy (2014)	1.36±0.010	±0.275	0.161	1.42±0.050	±0.652	0.198
Present	1.37±0.011	±0.333	0.164	1.40±0.049	±0.710	0.192

Table 2 Grid independence at Re=100

Number of Lagrangian points	$C_{d,mean}$	$C_{l,max}$	S_t	Number of Lagrangian points	$C_{d,mean}$	$C_{l,max}$	S_t
80	1.389	0.335	0.164	150	1.371	0.337	0.164
100	1.374	0.338	0.163	180	1.371	0.337	0.163
120	1.371	0.337	0.163	200	1.371	0.339	0.163

Table 3 Time-averaged force coefficients and Strouhal number for flow over a rotating cylinder (Re=100)

Study	η=0.5			η=1.0			η=1.5		
	C_d	C_l	S_t	C_d	C_l	S_t	C_d	C_l	S_t
Kang et al. (1999)	1.286	1.211	0.165	1.098	2.483	0.165	0.832	3.769	0.163
Stojkovic et al. (2002)	1.258	1.202	–	1.132	2.534	–	0.859	3.797	–
Yoon et al. (2009)	1.282	1.175	0.165	1.130	2.428	0.165	0.859	3.778	0.163
Present	1.315	1.167	0165	1.175	2.383	0.165	0.930	3.699	0.164

4 Numerical investigation of flow characteristics around two side-by-side cylinders

The incompressible flow past one cylinder is already considered as a classical case for validating IB-LBFS. However, there is some numerical research that uses non-body conforming Cartesian grid to simulate more complex structure or even engineering problems. As an extension to examine the ability of this numerical method to simulate more complicated geometrical configuration, flow around two side-by-side cylinders is studied in this section.

Flow past two stationary side-by-side cylinders is characterized by the interaction between the cylinder wakes that leads to a number of particular flow states depending upon the Reynolds number and gap spacing. Until now, the fluid dynamics of this problem has been examined experimentally (Alam et al., 2003; Alam and Zhou, 2007; Kim and Alam, 2015) and numerically (Afgan et al., 2011; Carini et al., 2014). Based on experimental observation, Williamson (1985) found three flow patterns characterized for the side-by-side arrangement for a low Reynolds number, i.e. $L<2.2D$, $2.2D\leq L<5D$, and $L\geq 5D$. The problem of flow past multiple moving bluff bodies has been paid great attention by many researchers. It is a great challenge for the traditional body-fitted numerical methods. As a representative case, flow past two counter-rotating cylinders has been simulated (Yoon et al., 2009; Chan and Jameson, 2010; Chan et al., 2011) and has shown that wake instabilities can be attenuated and even entirely suppressed.

In order to reflect the ability of IB-LBFS to solve incompressible flow, numerical simulations of flow past two stationary side-by-side cylinders are performed for three different gap spacings at low Reynolds numbers. Besides, numerical simulations of two rotating cylinders are performed with different normalized angular velocities, Reynolds number, and gap spacing. Once the reasonability and accuracy of simulation results by IB-LBFS are validated, it illustrates that IB-LBFS is an available alternative to the traditional numerical method and the process of solution is simple and convenient.

4.1 Flow past two stationary side-by-side cylinders

In this section, the results for the simulation of flow past two equal-sized stationary side-by-side cylinders are analyzed to reveal the effects of different flow parameters on the flow pattern. The effects of the variation in the Reynolds number and gap spacing on flow characteristics are analyzed by IB-LBFS. This study provides a better understanding of the wake structure around two-cylinder geometries. The results may show notable deviations from the results obtained for a fixed cylinder in terms of hydrodynamic forces, wake pattern, and vortex shedding from the cylinders.

Flow past two stationary cylinders with side-by-side arrangement is simulated in a $100D\times 80D$ rectangular domain as shown in Fig. 6. The rotational speed is set to zero. The centers of both cylinders are located at $40D$ from the inlet boundary, and $60D$ from the outlet boundary. Numerical simulations are performed for three different gap spacings of 1.5, 3, and 4 at Reynolds numbers of 100 and 200, respectively.

4.1.1 Flow past two stationary side-by-side cylinders at Re=100

Time histories of lift and drag forces for different gap spacings are depicted in Figs. 7–9 at Re=100. When the gap spacing is L/D=1.5, the lift and drag coefficients vary irregularly with time, implying that the flow is unsteady and non-periodic. The flow characteristics around two side-by-side cylinders at L/D=1.5 can also be observed from Fig. 10a. Along the streamline, we can see that at L/D=1.5, as time increases, the two wakes behind the cylinders merge into one main wake.

For the larger gap spacing (L/D=3.0 and L/D=4.0), time histories of lift and drag forces (Figs. 8 and 9) imply that the flow characteristics become periodic as time increases. As shown in the evolution of the force coefficients, the drag coefficient exists in a 180° phase difference at L/D=3.0 while in-phase at L/D=4.0. For the lift force, the trait of vortex shedding is in-phase (anti-symmetric about the flow centerline from the two cylinders) for L/D=3.0 and the trait of vortex shedding is anti-phase (symmetric about the flow centerline) for L/D=4.0.

The wakes of flow around two side-by-side cylinders are shown in Fig. 10b including streamlines, pressure and vorticity contours. Unlike the wakes with a small gap spacing that merge, the wakes with larger gap spacing form a flow separation. The modes of vortex shedding behind the cylinders can be observed,

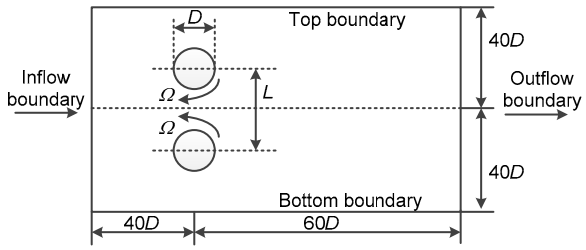

Fig. 6 Computational domain of two side-by-side cylinders

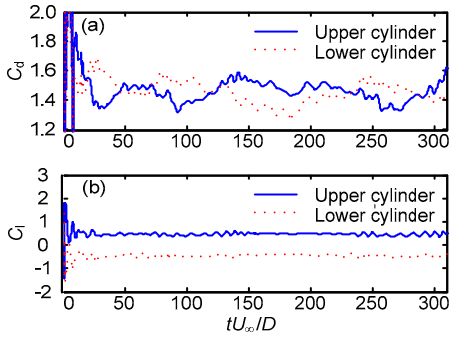

Fig. 7 Time histories of lift force (a) and drag force (b) for *Re*=100 and *L*/*D*=1.5

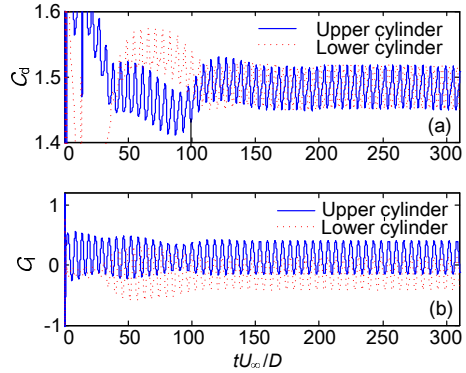

Fig. 8 Time histories of lift force (a) and drag force (b) for *Re*=100 and *L*/*D*=3

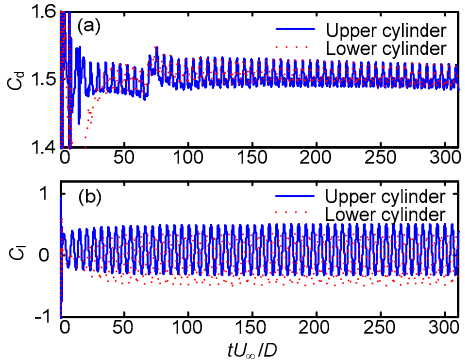

Fig. 9 Time histories of lift force (a) and drag force (b) for *Re*=100 and *L*/*D*=4

including in-phase or anti-phase synchronization of wakes in Figs. 10b and 10c. They show the asymmetric shedding of synchronized in-phase vortices from Fig. 10b and asymmetric shedding of synchronized anti-phase vortices in Fig. 10c. Besides, the two wake vortices of side-by-side cylinders merge into a bigger wake in the vertical direction at a distance downstream as time increases for *L*/*D*=3.0. On the contrary, two Karman vortex streets, which are symmetric along the centerline of the gap spacing, are clearly observed in Fig. 10c.

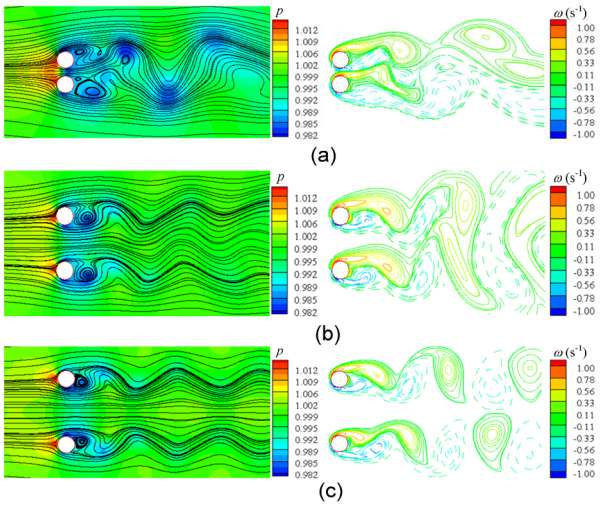

Fig. 10 Flow characteristics for two side-by-side cylinders (*Re*=100) on different gap spacings

(a) Streamlines and pressure contour (left) and vorticity contour (right) at *L*/*D*=1.5; (b) Streamlines and pressure contour (left) and vorticity contour (right) at *L*/*D*=3.0; (c) Streamlines and pressure contour (left) and vorticity contour (right) at *L*/*D*=4.0

4.1.2 Flow past two stationary side-by-side cylinders at *Re*=200

Time histories of lift and drag forces for different gap spacings are depicted in Figs. 11–13 at *Re*=200. When the gap spacing is *L*/*D*=1.5, the lift and drag coefficients imply that the flow is unsteady and non-periodic and similar to *Re*=100. It can be also seen from Fig. 14a, which shows the flow characteristics for two side-by-side cylinders on *L*/*D*=1.5.

Differ from the force coefficients at *Re*=100, for the larger gap spacing, the evolutions of the drag are both in-phase and synchronous and the evolutions of the lift are anti-phase at *L*/*D*=3.0 and 4.0. The average drag coefficient at *Re*=200 is slightly greater than that at *Re*=100 at *L*/*D*=1.5 and 3.0 while the drag is

slightly smaller at *Re*=200 and *L*/*D*=4.0. The maximum absolute value of the lift coefficient at *Re*=200 is more than that at *Re*=100.

The wakes are shown in Figs. 14b and 14c including streamlines, pressure, and vorticity contours. The wakes are formed separately in the larger gap spacing. In Figs. 14b and 14c, the mode of vortex shedding behind the cylinders can be observed. It consists of asymmetric shedding of synchronized anti-phase vortices. Moreover, two Karman vortex streets, which are symmetric along the centerline of the gap spacing, are clearly observed.

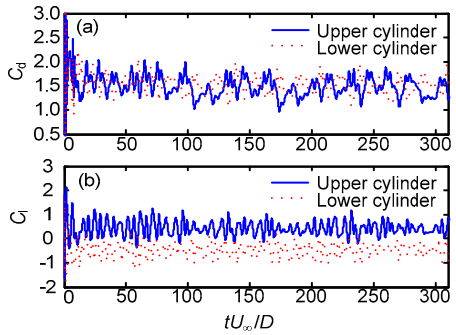

Fig. 11 Time histories of lift force (a) and drag force (b) for *Re*=200 and *L*/*D*=1.5

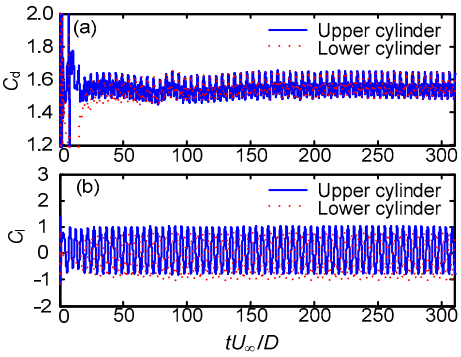

Fig. 12 Time histories of lift force (a) and drag force (b) for *Re*=200 and *L*/*D*=3.0

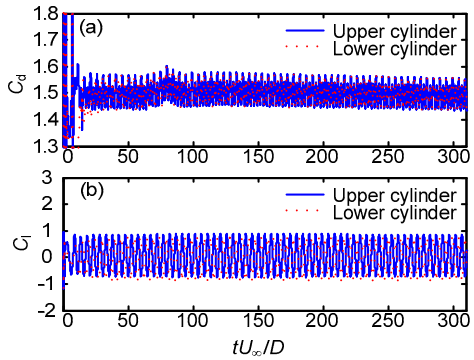

Fig. 13 Time histories of lift force (a) and drag force (b) for *Re*=200 and *L*/*D*=4.0

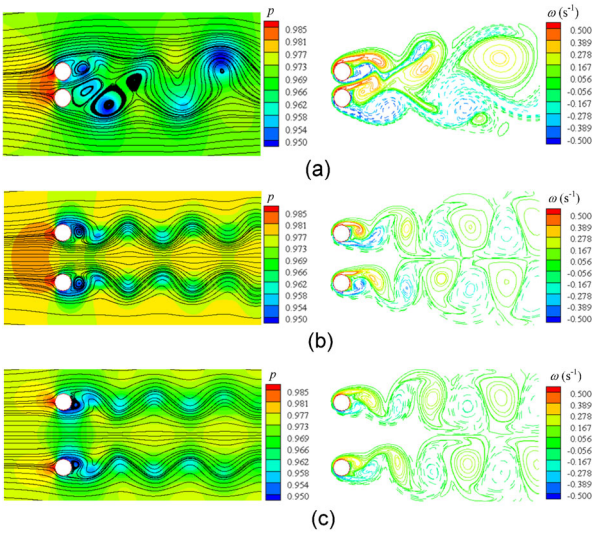

Fig. 14 Flow characteristics for two side-by-side cylinders (*Re*=200) on different gap spacings

(a) Streamlines and pressure contour (left) and vorticity contour (right) at *L*/*D*=1.5; (b) Streamlines and pressure contour (left) and vorticity contour (right) at *L*/*D*=3.0; (c) Streamlines and pressure contour (left) and vorticity contour (right) at *L*/*D*=4.0

Based on the above results, the small gap induces a biased flow and forms an irregular big wake behind two cylinders. As the gap increases, the biased flow vanishes and less wake interaction is observed, implying that both cylinders behave independently.

4.2 Flow past two rotating side-by-side circular cylinders

In the present simulations, the effects of the main important parameters on flow characteristics are analyzed, including the normalized angular velocity, Reynolds number, and gap spacing. The computational domain is shown in Fig. 6.

4.2.1 Effect of rotational speed and Reynolds number on flow characteristics

In this section, the results for numerical simulations of flow past two rotating side-by-side cylinders, where the gap spacing between the two cylinders is *L*/*D*=2, are analyzed to reveal the effects of different normalized angular velocity on the flow pattern. Two side-by-side rotating cylinders of the same diameter are placed in a free stream. The following parameters are: ρ=1.0, U_∞=0.1, and *D*=1.0. Three Reynolds numbers of 100, 150, and 200 are applied in these simulations. Six different rotational speeds of 0.5, 1.0,

1.5, 2.0, 2.5, and 3.0 are applied to examine their effects on the flow pattern.

The time-averaged values of the drag and lift coefficients for the upper cylinder (L/D=2.0) with various values of rotational speed at three Reynolds numbers are shown in Table 4. The results are compared with the numerical results in (Chan et al., 2011) and good agreements are obviously achieved. It can be seen that the time-averaged drag coefficient generally decreases with increasing normalized rotational speed. It was found that the mean lift coefficient increases with increasing rotational speed. Additionally, the low Reynolds number has little effect on force coefficients.

Fig. 15 shows the streamlines for flow past two side-by-side rotating cylinders at L/D=2.0 and different rotational speeds and different Reynolds numbers. When Re=100, the flow appears irregular and unsteady at η=0.5 and 1.0 as shown in Fig. 15a. Then, vortex shedding suppression occurs as normalized rotational speed increases. The unsteady wakes behind the cylinders can be completely suppressed and symmetrical flow patterns are formed when η=3.0. From Figs. 15b and 15c, the unsteady wakes behind the cylinders also can be seen at η=0.5, 1.0, and 1.5 for Re=150 and 200, respectively. Moreover, the unsteady wakes can be suppressed and the flow becomes steady with increase in the rotational speed.

4.2.2 Effect of gap spacing on flow characteristics

In this section, the numerical simulation results for flow past two rotating side-by-side cylinders are analyzed to reveal the effects of different gap spacings on the flow pattern. Two side-by-side rotating cylinders of the same diameter are placed in a free stream at a Reynolds number of 200. The following parameters are: ρ=1.0, U_∞=0.1, D=1.0, and η=1.0. Five different gap spacings of L/D=1.2, 1.5, 1.8, 2.0, and 2.5 are applied to examine their effects on the flow patterns.

The time histories of drag and lift coefficients for flow past two side-by-side rotating cylinders (Re=200) at three different gap spacings are shown in Fig. 16, and Figs. 17 and 18 (p.396), respectively. The streamlines and vorticity contours are shown in Fig. 19. It can be seen that the near-wake structure behind two circular cylinders in a side-by-side configuration mainly consists of three different configurations, depending on the value of L/D. In the case of L/D=1.2, the flow characteristic is similar to the flow past a single cylinder, with vortices being alternately shed. The flow between the two cylinders appears as a very thin streak of high momentum fluid, which is wrapped around either of the two cylinders. In the case of L/D=1.2, 1.5, and 2.0, the flow shows an unsteady and bistable behavior of the wake. The flow between the two cylinders is intermittently deflected to either of the two cylinders. Then, as the gap spacing increases, two separate vortex streets are formed, which are coupled with a definite phase relationship and a single shedding frequency.

Table 4 Time-averaged values of the drag and lift coefficients for the upper cylinder (L/D=2.0)

Re	Force coefficient	Study	Time-averaged value					
			η=0.5	η=1.0	η=1.5	η=2.0	η=2.5	η=3.0
100	C_d	Chan et al. (2011)	1.153	0.836	0.496	0.224	−0.008	−0.005
		Present	1.154	0.809	0.525	0.258	0.033	0.016
	C_l	Chan et al. (2011)	1.370	2.533	3.771	5.127	6.585	6.127
		Present	1.371	2.508	3.666	4.952	6.416	6.925
150	C_d	Chan et al. (2011)	1.151	0.780	0.459	0.168	−0.024	0.003
		Present	1.225	0.833	0.508	0.200	0.005	0.016
	C_l	Chan et al. (2011)	1.311	2.441	3.673	5.023	6.520	6.078
		Present	1.381	2.448	3.514	4.862	6.411	6.804
200	C_d	Chan et al. (2011)	1.150	0.766	0.417	0.133	−0.038	−0.002
		Present	1.347	0.897	0.438	0.166	−0.007	0.012
	C_l	Chan et al. (2011)	1.335	2.434	3.740	4.986	6.615	6.070
		Present	1.339	2.428	3.467	4.790	6.402	6.851

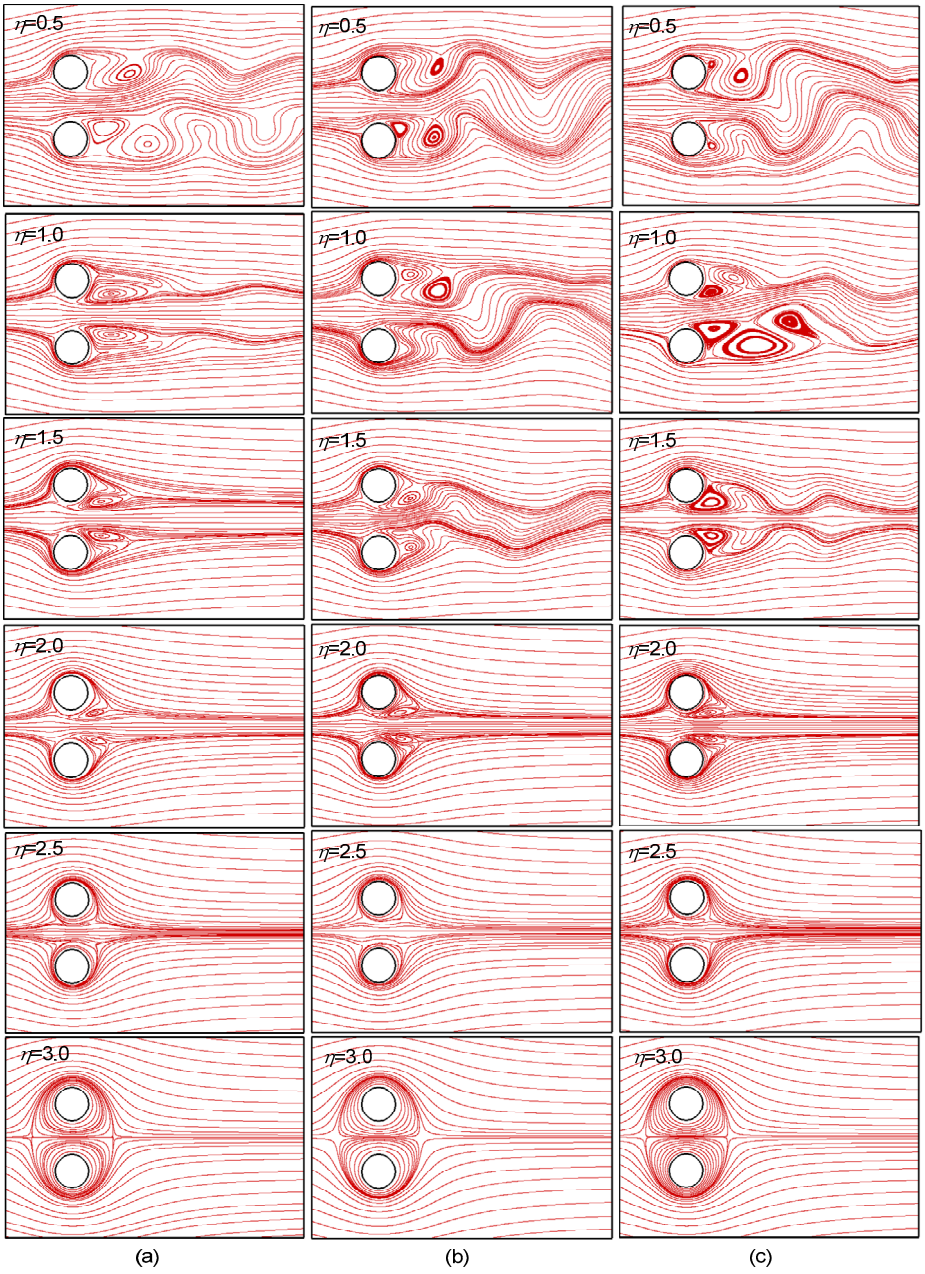

Fig. 15 Streamlines for flow past two side-by-side rotating cylinders at L/D=2.0 at different rotational speeds
(a) Re=100; (b) Re=150; (c) Re=200

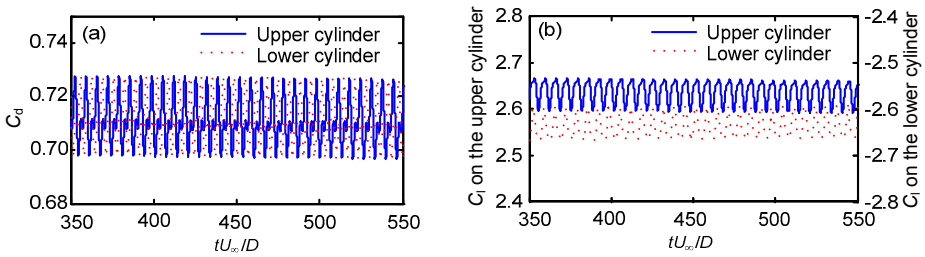

Fig. 16 Time histories of drag (a) and lift (b) coefficients for Re=200 and L/D=1.2

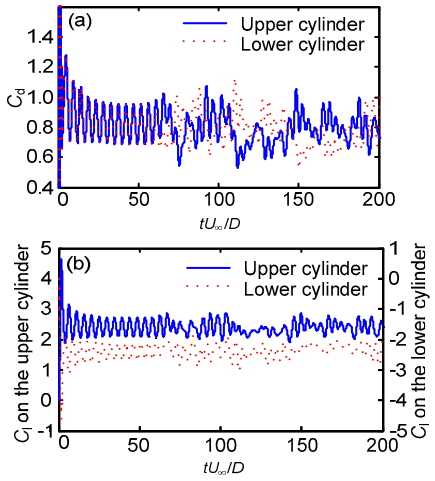

Fig. 17 Time histories of drag (a) and lift (b) coefficients for *Re*=200 and *L*/*D*=1.8

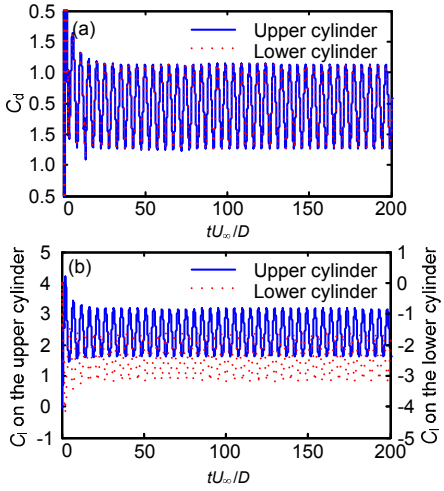

Fig. 18 Time histories of drag (a) and lift (b) coefficients for *Re*=200 and *L*/*D*=2.5

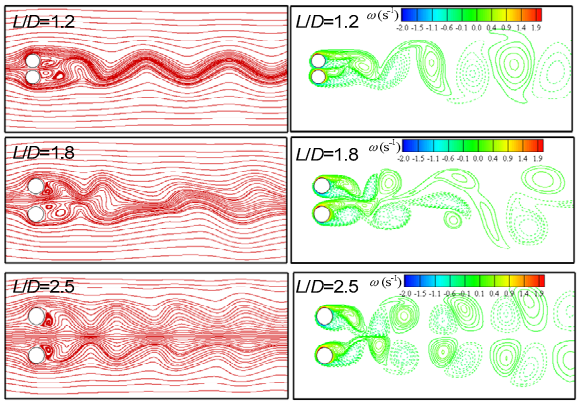

Fig. 19 Streamlines and vorticity contours for flow past two side-by-side rotating cylinders at *Re*=200 and different gap spacings

5 Conclusions

The unsteady incompressible viscous flows around two stationary and rotating circular cylinders with side-by-side arrangement are numerically simulated to study the flow characteristics by IB-LBFS. Differing from the traditional numerical method, which solves macroscopic equations using a body-fitted mesh, IB-LBFS can evaluate its viscous and inviscid fluxes simultaneously by local reconstruction of the LBE solutions and solves the governing equations with a non-body conforming Cartesian grid by using IB technique. Therefore, the overall solution process is considerably simplified, especially for solving moving boundary problems. In this study, IB-LBFS is validated as an available alternative for simulating the flow past multiple bluff bodies.

For flow past two stationary side-by-side cylinders at a low Reynolds number, the simulation results show that the wake is irregular at small gap spacing. As the gap increases, the biased flow vanishes and there is less wake interactions until the in-phase or anti-phase flow is observed. The Reynolds number also affects the value of the force coefficients.

For flow past two rotating side-by-side cylinders, the simulation results illustrate that a low Reynolds number has little effect on the force coefficients. The rotational speed, as the main important parameter, affects flow characteristics. As the numerical results illustrate, with increasing rotational speed the unsteady wakes can be suppressed and the flow becomes steady. Furthermore, the wake structure is affected by the gap spacing. At small gap spacing, the flow is unsteady and intermittently deflected to each of the two cylinders. As the gap spacing increases, two separate vortex streets behind each cylinder are formed with a definite phase relationship and a single shedding frequency.

References

Afgan I, Kahil Y, Benhamadouche S, et al., 2011. Large eddy simulation of the flow around single and two side-by-side cylinders at subcritical Reynolds numbers. *Physics of Fluids*, 23(7):075101. https://doi.org/10.1063/1.3596267

Alam MM, Moriya M, Sakamoto H, 2003. Aerodynamic characteristics of two side-by-side circular cylinders and application of wavelet analysis on the switching phenomenon. *Journal of Fluids and Structures*, 18(3-4): 325-346.

https://doi.org/10.1016/j.jfluidstructs.2003.07.005

Alam MM, Zhou Y, 2007. Flow around two side-by-side closely spaced circular cylinders. *Journal of Fluids and Structures*, 23(5):799-805. https://doi.org/10.1016/j.jfluidstructs.2006.12.002

Behzad GD, Hamed HG, 2009. Numerical simulation of flow through tube bundles in in-line square and general staggered arrangements. *International Journal of Numerical Methods for Heat and Fluid Flow*, 19(8):1038-1062. https://doi.org/10.1108/09615530910994487

Carini M, Giannetti F, Auteri F, 2014. On the origin of the flip-flop instability of two side-by-side cylinder wakes. *Journal of Fluid Mechanics*, 742:552-576. https://doi.org/10.1017/jfm.2014.9

Chan AS, Jameson A, 2010. Suppression of the unsteady vortex wakes of a circular cylinder pair by a doublet-like counter-rotation. *International Journal for Numerical Methods in Fluids*, 63(1):22-39. https://doi.org/10.1002/fld.2075

Chan AS, Dewey PA, Jameson A, et al., 2011. Vortex suppression and drag reduction in the wake of counter-rotating cylinders. *Journal of Fluid Mechanics*, 679: 343-382. https://doi.org/10.1017/jfm.2011.134

Choi JI, Oberoi RC, Edwards JR, et al., 2007. An immersed boundary method for complex incompressible flows. *Journal of Computational Physics*, 224(2):757-784. https://doi.org/10.1016/j.jcp.2006.10.032

Ding H, Shu C, Yeo KS, et al., 2007. Numerical simulation of flows around two circular cylinders by mesh-free least square-based finite difference methods. *International Journal for Numerical Methods in Fluids*, 53(2):305-332. https://doi.org/10.1002/fld.1281

Feng ZG, Michaelides EE, 2004. The immersed boundary-lattice Boltzmann method for solving fluid-particles interaction problems. *Journal of Computational Physics*, 195(2):602-628. https://doi.org/10.1016/j.jcp.2003.10.013

Feng ZG, Michaelides EE, 2005. Proteus: a direct forcing method in the simulations of particulate flows. *Journal of Computational Physics*, 202(1):20-51. https://doi.org/10.1016/j.jcp.2004.06.020

Gao YY, Yu DY, Tan S, et al., 2010. Experimental study on the near wake behind two side-by-side cylinders of unequal diameters. *Fluid Dynamics Research*, 42(5):055509. https://doi.org/10.1088/0169-5983/42/5/055509

Harichandan AB, Roy A, 2010. Numerical investigation of low Reynolds number flow past two and three circular cylinders using unstructured grid CFR scheme. *International Journal of Heat and Fluid Flow*, 31(2):154-171. https://doi.org/10.1016/j.ijheatfluidflow.2010.01.007

Hesam SM, Navid N, Behzad GD, 2011. Numerical simulation of flow over two side-by-side circular cylinder. *Journal of Hydrodynamics, Ser. B*, 23(6):792-805. https://doi.org/10.1016/S1001-6058(10)60178-3

Kang S, Choi H, Lee S, 1999. Laminar flow past a rotating cylinder. *Physics of Fluids*, 11(11):3312-3321. https://doi.org/10.1063/1.870190

Kim S, Alam MM, 2015. Characteristics and suppression of flow-induced vibrations of two side-by-side circular cylinders. *Journal of Fluids and Structures*, 54:629-642. https://doi.org/10.1016/j.jfluidstructs.2015.01.004

Kumar S, Gonzalez B, Probst O, 2011. Flow past two rotating cylinders. *Physics of Fluids*, 23(1):014102. https://doi.org/10.1063/1.3528260

Lai MC, Peskin CS, 2000. An immersed boundary method with formal second-order accuracy and reduced numerical viscosity. *Journal of Computational Physics*, 160(2): 705-719. https://doi.org/10.1006/jcph.2000.6483

Liu C, Zheng X, Sung CH, 1998. Preconditioned multigrid methods for unsteady incompressible flows. *Journal of Computational Physics*, 139(1):35-57. https://doi.org/10.1006/jcph.1997.5859

Mohany A, Arthurs D, Bolduc M, et al., 2014. Numerical and experimental investigation of flow-acoustic resonance of side-by-side cylinders in a duct. *Journal of Fluids and Structures*, 48:316-331. https://doi.org/10.1016/j.jfluidstructs.2014.03.015

Qian YH, D'Humières D, Lallemand P, 1992. Lattice BGK model for Navier-Stokes equation. *Europhysics Letters (EPL)*, 17(6):479-484. https://doi.org/10.1209/0295-5075/17/6/001

Shu C, Wang Y, Teo CJ, et al., 2015. Development of lattice Boltzmann flux solver for simulation of incompressible flows. *Advances in Applied Mathematics and Mechanics*, 6(04):436-460. https://doi.org/10.4208/aamm.2014.4.s2

Song FL, Tseng SY, Hsu SW, et al., 2015. Gap ratio effect on flow characteristics behind side-by-side cylinders of diameter ratio two. *Experimental Thermal and Fluid Science*, 66:254-268. https://doi.org/10.1016/j.expthermflusci.2015.04.001

Stojkovic D, Breuer M, Durst F, 2002. Effect of high rotation rates on the laminar flow around a circular cylinder. *Physics of Fluids*, 14(9):3160-3178. https://doi.org/10.1063/1.1492811

Supradeepan K, Roy A, 2014. Characterisation and analysis of flow over two side by side cylinders for different gaps at low Reynolds number: a numerical approach. *Physics of Fluids*, 26(6):063602. https://doi.org/10.1063/1.4883484

Supradeepan K, Roy A, 2015. Low Reynolds number flow characteristics for two side-by-side rotating cylinders. *Journal of Fluids Engineering*, 137(10):101204. https://doi.org/10.1115/1.4030486

Vakil A, Green SI, 2011. Two-dimensional side-by-side circular cylinders at moderate Reynolds numbers. *Computers & Fluids*, 51(1):136-144. https://doi.org/10.1016/j.compfluid.2011.08.008

Wang Y, Shu C, Teo CJ, et al., 2015a. An immersed boundary-lattice Boltzmann flux solver and its applications to fluid-

structure interaction problems. *Journal of Fluids and Structures*, 54:440-465.
https://doi.org/10.1016/j.jfluidstructs.2014.12.003

Wang Y, Shu C, Huang HB, et al., 2015b. Multiphase lattice Boltzmann flux solver for incompressible multiphase flows with large density ratio. *Journal of Computational Physics*, 280:404-423.
https://doi.org/10.1016/j.jcp.2014.09.035

Wang Y, Shu C, Teo CJ, et al., 2016. An efficient immersed boundary-lattice Boltzmann flux solver for simulation of 3D incompressible flows with complex geometry. *Computers & Fluids*, 124:54-66.
https://doi.org/10.1016/j.compfluid.2015.10.009

Wang Y, Shu C, Yang LM, et al., 2017. On the immersed boundary-lattice Boltzmann simulations of incompressible flows with freely moving objects. *International Journal for Numerical Methods in Fluids*, 83(4):331-350.
https://doi.org/10.1002/fld.4270

Wang ZJ, Zhou Y, 2005. Vortex interactions in a two side-by-side cylinder near-wake. *International Journal for Heat and Fluid Flow*, 26(3):362-377.
https://doi.org/10.1016/j.ijheatfluidflow.2004.10.006

Williamson CHK, 1985. Evolution of a single wake behind a pair of bluff bodies. *Journal of Fluid Mechanics*, 159: 1-18.
https://doi.org/10.1017/S002211208500307X

Wu J, Shu C, 2009. Implicit velocity correction-based immersed boundary-lattice Boltzmann method and its applications. *Journal of Computational Physics*, 228(6): 1963-1979.
https://doi.org/10.1016/j.jcp.2008.11.019

Wu J, Shu C, 2010. An improved immersed boundary-lattice Boltzmann method for simulating three-dimensional incompressible flows. *Journal of Computational Physics*, 229(13):5022-5042.
https://doi.org/10.1016/j.jcp.2010.03.024

Yoon HS, Chun HH, Kim JH, et al., 2009. Flow characteristics of two rotating side-by-side circular cylinder. *Computers & Fluids*, 38(2):466-474.
https://doi.org/10.1016/j.compfluid.2008.09.002

中文概要

题　目: 基于浸入边界-格子波尔兹曼通量求解法的并列双圆柱流动特性数值研究

目　的: 本文旨在应用新型数值求解方法，即浸入边界-格子波尔兹曼通量求解法，研究并列双圆柱流动特性，并探索该数值方法在工程应用中的可行性。

创新点: 1. 将浸入边界法与格子波尔兹曼求解法相结合，简单并高效地实现在非均匀直角网格下求解不可压流动以及动边界问题；2. 应用浸入边界-格子波尔兹曼求解法研究并列双圆柱流场特性。

方　法: 1. 通过理论推导，建立状态变量和通量与格子波尔兹曼方程中粒子密度分布函数之间的关系（公式（8）~（10））；2. 采用强制浸入边界法处理流固界面使固壁表面满足无滑移边界条件，实现在笛卡尔网格下求解运动边界问题；3. 通过数值模拟，探讨雷诺数和圆柱间距对静止双圆柱受力及流场尾流特性的影响以及雷诺数、间距和旋转速度对旋转并列双圆柱受力及尾流特性的影响规律。

结　论: 1. 浸入边界-格子波尔兹曼求解法可以简单实现采用非贴体网格求解不可压流动及动边界问题。2. 对于并列静止双圆柱，随着间距的增加，双圆柱尾流场的相互作用逐渐消失，尾迹由无规则性转变为规则的同相位流动或反向流动；雷诺数影响圆柱受力系数。3. 对于并列旋转双圆柱，雷诺数对旋转圆柱受力影响较弱；旋转速度可以抑制单圆柱尾流场的非定常效应；随着圆柱间距的增加，双圆柱后方形成固定的相位关系以及同一频率的脱落涡。

关键词: 浸入边界法；格子波尔兹曼通量求解法；运动边界；并列圆柱